



Fabrication of novel all-solid-state Z-scheme heterojunctions of 3DOM-WO₃/Pt coated by mono-or few-layered WS₂ for efficient photocatalytic decomposition performance in Vis-NIR region

Xiaoqing Yan, Mengyang Xia, Baorong Xu, Jinjia Wei, Bolun Yang, Guidong Yang*

XJTU-Oxford Joint International Research Laboratory of Catalysis, School of Chemical Engineering and Technology, Xi'an Jiaotong University, Xi'an, Shaanxi 710049, China

ARTICLE INFO

Keywords:

3DOM
Z-scheme heterojunction
Mono-or few-layered WS₂
Gas phase chemical reduction
Wastewater purification

ABSTRACT

In this work, novel three dimensional ordered macroporous (3DOM) WO₃/Pt/WS₂ all-solid-state Z-scheme heterojunctions were firstly synthesized by gas phase chemical reduction methods. The layer numbers of coated WS₂ on the skeleton of 3DOM Z-scheme heterojunctions are easily tuned by controlling the amount of sulfur powder, and the energy band structure of WS₂ can be thus artificial turned, leading to distinct visible and near infrared (Vis-NIR) light absorption and charge separation ability of the as-prepared 3DOM samples. The experimental results show that the obtained 3DOM-WO₃/Pt sample coated by 2–3 layered WS₂ exhibits high photoelectric conversion ability, unbelievable photocurrent signal and excellent photodegradation activity, suggesting that the high separation efficiency of photon-generated charge can result in the superior photocatalytic performance of 3DOM-WO₃/Pt/WS₂. The selective photo-deposition of Au is used to proof the possible mechanism of charges transfer, and the results show that Z-scheme heterojunction can endow 3DOM-WO₃/Pt/WS₂ sample with a unique charges migration path, in which the photogenerated electrons on the conduction band (CB) of WO₃ and the holes on the valence band (VB) of WS₂ are easily transferred into metal Pt to recombine and the lifetime of electrons on the CB of WS₂ as well as the holes on the VB of WO₃ are strongly prolonged.

1. Introduction

In recent years, transition metal dichalcogenides (TMDs) are attracting much attention owing to their advanced physicochemical and optical properties [1–5], which thus have been deeply investigated and potential applied in the field of photocatalysis. However, the traditional bulk TMDs show poor photocatalytic activity for wastewater cleaning due to the fact that the charge carriers excited by solar energy just directly convert into heat rather than take part in the photoreaction [6]. Fortunately, the recent studies have been found that when the bulk TMDs were reduced to mono-or few-layered structure, its electronic and optical properties can be amazingly changed [7–10]. This is because mono-or few-layered TMDs possess graphene-like layered structure with the unique layer-dependent properties and that greatly differ from the feature of the bulk materials [1,11]. Therefore, the monolayer TMDs, as a novel nanosheet structure, have opened up more opportunities for the design and synthesis of high-efficiency semiconductor materials in application of photocatalysis [12,13], optoelectronics devices [14], and lithium-ion batteries [15,16].

WS₂, as a typical TMDs photocatalyst, is characterized by strong covalent bonding in-plane and weak non-covalent bonding between layer and layer [17,18]. When the bulk WS₂ was reduced to monolayer WS₂, its bulk indirect bandgap of 1.4 eV would increase to a direct bandgap of about 2.2 eV in single-layer form [5,19]. At the same time, its corresponding electronic and optical properties are changed greatly [20,21]. For example, based on the theoretical calculation method, Liu et al. [22] have concluded that the monolayer WS₂ showed the highest on-state current density and mobility compared with other common TMDs (such as MoS₂, MoSe₂, WSe₂). Sang et al. [6] have reported that the pure WS₂ nanosheets exhibited an excellent photodegradation activity from UV to near-infrared light. Morrish et al. [23] have prepared WS₂ thin films by H₂S sulfurization of WO₃ at low temperature, which can vastly reduce the overpotential for HER.

Recently, lots of studies have reported that the construction of novel Z-scheme heterojunction is one of promising techniques to significantly enhance the separation of electron-hole pairs, resulting in much high photocatalytic activity of WS₂ [24,25]. It is well known that WO₃ and mono-or few-layered WS₂ possess very similar chemical property and

* Corresponding author.

E-mail address: guidongyang@xjtu.edu.cn (G. Yang).

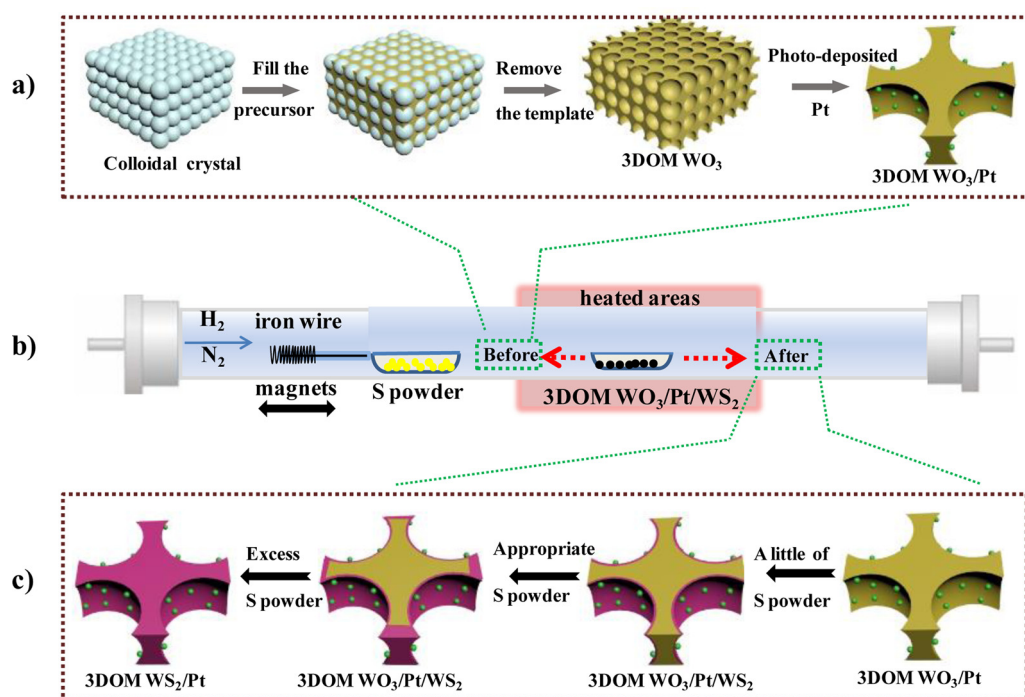


Fig. 1. (a) Formation route of 3DOM-WO₃/Pt. (b) sulfuration process in the quartz tube. (c) fabrication mechanism of the 3DOM-WO₃/Pt/WS₂.

matched band structure, allowing to create the lateral Z-scheme heterojunction without inducing structural defects. In this kind of WO₃/WS₂ heterostructured system, the recombination of photogenerated electron-hole pairs can be significantly suppressed and the light absorption performance in Vis-NIR region is synchronously enhanced [26]. More importantly, the auxiliary WO₃ with a deeper valence band (+3.1 eV) can potentially enhance the water oxidation ability, and all of the above advantages synergistically lead to the excellent photodegradation activity of the WO₃/WS₂ system [27]. In recent years, a large numbers of works have been delivered that the special morphological structure has the significant effect on the high photocatalytic activity of semiconductor photocatalyst, which not only can enhance the specific surface area to enrich the reaction active sites, but also can promote the visible light absorption as well as the separation of electron-hole pairs [28–30]. Among them, three dimensional ordered macroporous semiconductor photocatalysts, as a class of important porous structured materials, have attracted much more attentions due to their structure advantages in the utilization of photocatalysis. This advanced architecture with an interconnected macroporous network can facilitate the mass transfer, provide large active surface area and enhance the light energy conversion efficiency produced by the effect of slow photon and multiple scattering [31,32]. However, to date, few works has been reported on the creation of all-solid-state Z-scheme heterojunction of 3DOM-WO₃/Pt/WS₂. It is thus expected that this kind of photocatalysts perform very well on environmental purification under Vis-NIR light irradiation.

Inspired by above motivation, we, for the first time, demonstrated a simple approach to create the all-solid-state Z-scheme heterojunction of 3DOM-WO₃/Pt/WS₂ by gas phase chemical reduction methods. The layer numbers of coated WS₂ on the skeleton surface of 3DOM-WO₃/Pt materials can be effectively tuned by controlling the amount of sulfur powder, which has a significant effect on the energy band structure and the light absorption ability of the as-prepared 3DOM-WO₃/Pt/WS₂ photocatalyst. As a result, the novel all-solid-state Z-scheme heterojunction exhibits highly photocatalytic performance, and among these obtained samples, the sample of 3DOM-WO₃/Pt coated by 2–3 layered WS₂ exhibits the strongest separation efficiency of photogenerated electron-hole pairs, and thus leading to the best photocatalytic activity.

In addition, the photocatalytic reaction mechanism and the electrons migration path in the Z-scheme heterojunction were discussed according to the characterization results.

2. Experimental section

2.1. Preparation of the 3DOM-WO₃

3DOM metal oxides were fabricated by colloidal crystal templating method [33,34]. Up to date, the raw materials of tungsten chloride, tungsten ethoxide or ammonium metatungstate was used to synthesize 3DOM-WO₃ [35–37]. Although these materials can well prepare 3DOM-WO₃, the cost of tungsten source are very expensive. Therefore, in this study, we successfully use tungstic acid as common and cheap raw material to synthesize 3DOM-WO₃. In brief, 1.0 g tungstic acid was dissolved into 40 mL deionized water with 0.8 mL ammonium hydroxide under continuously stirring at room temperature. After about 5 h, the mixed solution would become a transparent solution. And then, 1.26 g oxalic acid was added. Until the oxalic acid was absolutely dissolved, 3 g PMMA was immersed into the above mixture solution and dried at 80 °C for 12 h in the vacuum drying oven. Finally, the sample was calcined in air at a ramp of 1 °C/min from room temperature to 500 °C and maintained for 3 h, and thus the pure 3DOM-WO₃ was obtained.

2.2. Preparation of 3DOM-WO₃/Pt sample

3 wt% of Pt was in-situ photo-deposited onto the surface of 3DOM-WO₃. In every reaction, 0.3 g 3DOM-WO₃ was dispersed in the mixed solution containing 40 mL deionized water, 4 mL lactic acid (the hole scavenger) and 2.4 mL 1 wt% H₂PtCl₆ solution. And then, the mixed solution was irradiated by 300 W xenon lamp for 3 h with constantly stirring. After centrifugation and washing with deionized water for several times, the resulting production was then dried at 60 °C to obtain 3DOM-WO₃/Pt.

2.3. Preparation of 3DOM-WO₃/Pt/WS₂ Z-scheme heterojunction

In the quartz tube, 0.15 g 3DOM-WO₃/Pt was put in the middle area of furnace and sulfur powder was placed in the front of 3DOM-WO₃/Pt sample (Fig. 1b). Hydrogen as the carrying gas was then filled into the quartz tube before the tube furnace was turned on. The rate of hydrogen was keeping constant (200 mL/min) and the furnace reached to the desired temperatures (550 °C) with a constant rate of 20 °C/min. After 10 min reaction, the powdered sulfur was moved away heated areas by magnet. Then, the carrying gas was changed to high purity nitrogen, which was used to cool the reactor and thus obtain the 3DOM-WO₃/Pt/WS₂ Z-scheme samples. The samples prepared with different sulfur powder amount of 0.015 g, 0.0300 g, 0.0450 g, 0.0600 g and 0.1500 g were denoted as WOS-1, WOS-2, WOS-3, WOS-4, and 3DOM-WS₂/Pt, respectively.

2.4. Characterizations

The surface morphology and inner geometry of all as-prepared photocatalysts were examined by the field-emission scanning electron microscope (SEM, JEOL, JSM-6700F) and the transmission electron microscopy (TEM, JEOL, JEM-2100), respectively. The powder X-ray diffraction was tested by SHIMADZU Lab X XRD-6100, and the 2θ range was scanned from 10 °C to 80 °C. The photoluminescence spectra were recorded on an Edinburgh instruments FLS980 fluorescence spectrophotometer with exciting wavelength of 325 nm. And the optical adoption properties were analyzed by using a Hitachi U-4100 UV/Vis spectrometer. The X-ray photoelectron spectroscopy (XPS) was tested by Kratos AXIS Ultra Dld photoelectron spectrometer with monochromatic Al-Kα excitation ($h\nu = 1486.69$ eV), the bonding energies were calibrated by the C 1s internal standard peak at 285.0 eV. In addition, the specific surface area and pore size distribution plots of the samples were analyzed by nitrogen adsorption-desorption apparatus (BET, BELsorp).

2.5. Evaluation of photocatalytic activity

2.5.1. Pollutant degradation

The photodegradation pollution activity of the samples was evaluated by the removal of the 30 mg/L RhB dye solution. The simulated Vis-NIR light source was 300 W Xenon lamp (NBeT, HSX-F300, Beijing) and the cut-off glass filter ($\lambda > 420$ nm) was used to permit only Vis-NIR light to go through. In order to reach the absorption/desorption equilibrium, 30 mg of the photocatalysts should be firstly added into 60 mL solution contained 30 mg L⁻¹ of RhB, and then the mixed solution was continuously stirred for 40 min in the dark environment. After that, the continuously stirred mixed solution was exposed under Vis-NIR light irradiation. In the process of reaction, 3 mL of the solution was taken out every 5 min interval, and then the photocatalyst in solution was removed by centrifuging. Finally, the residual solution was tested by UV-vis spectrophotometer (UV-1900PPC, Shanghai, China).

2.5.2. Photocatalytic H₂ evolution

Hydrogen production from water splitting over the as-prepared photocatalysts was performed in a Pyrex reaction cell under Vis-NIR light irradiation. Typically, 0.05 g photocatalyst was dispersed in 50 mL deionized water with 10 mL triethanolamine under continuously stirring at room temperature. Prior to irradiation, the system was degassed with highly pure nitrogen for 15 min to remove the air inside. Finally the amount of H₂ generated was detected by gas chromatography (Beifen-Ruili, SP-2100A, China).

3. Results

Gas phase chemical reduction method is an effective way to prepare 3DOM-WO₃/Pt/WS₂ all-solid-state Z-scheme heterojunction

photocatalyst [38–40]. Fig. 1a shows the schematic illustration for the synthetic strategy of 3DOM-WO₃/Pt sample. Firstly, we use the emulsifier-free emulsion polymerization technique to obtain the mono-dispersed PMMA microspheres [28,33], and then the PMMA colloidal crystal template can be produced by centrifugation. Next, the precursor solution consisted of tungstic acid, oxalic and ammonium hydroxide were immersed into the gap of PMMA template under the vacuum drying state for reaction. And after calcination at 500 °C, the 3DOM-WO₃ can be successively obtained. Additionally, the Pt NPs were then loaded and highly dispersed on the surface of 3DOM-WO₃ by photo-deposited method. After that, the samples of 3DOM-WO₃/Pt and sulfur powder were synchronously located into the quartz tube as shown in Fig. 1b. Under high temperature, the sulfur powder reacted with H₂ to form H₂S, and which can easily reduce the 3DOM-WO₃/Pt to produce the 3DOM-WO₃/Pt/WS₂ heterojunction. As shown in Fig. 1c, the layer numbers of WS₂ on the 3DOM skeleton can be conveniently adjusted by the change of sulfur powder amount, if much more sulfur powder loading, the pure 3DOM-WS₂/Pt can be obtained.

The microstructure and morphology of the obtained samples were carefully investigated by scanning electron microscopy (SEM) and transmission electron microscopy (TEM). A general view of these as-prepared samples was shown in the Fig. 2a–g. It can be seen that the 3DOM-WO₃, 3DOM-WO₃/Pt, 3DOM-WS₂/Pt and 3DOM-WO₃/Pt/WS₂ Z-scheme photocatalysts exhibit similarly inverse opals structure, all of which possess well-defined macroporous networks and periodicity 3D-interconnected walls. This is because that the precursor of WO₃ had been replicated the closely-packed PMMA opals when the PMMA template was removed by calcining. The insets of Fig. 2a–g show the TEM images of the 3DOM samples. It can be clearly observed that all the samples show a well-defined three dimensionally ordered macroporous structure with diameters of approximately 300 nm, and no significant difference was found in the microstructure among these samples, indicating that the process of photo-deposition Pt and sulfuration by H₂S gas was not given rise to the collapse of 3DOM shapes. Fig. 2h–i shows the selected area electron diffraction (SAED) patterns of 3DOM-WO₃ and WOS-2 samples. The 3DOM-WO₃ sample has a clear polycrystalline ring, indicating the well crystalline degree of WO₃. While the WOS-2 sample shows a weak diffraction ring and some diffraction spots can be observed simultaneously, which is indexed to the existence of WO₃ and single-crystalline WS₂ in the 3DOM composites. This phenomenon is in accordance with XRD analysis.

The microscopic surface structures of the obtained samples were further studied by the high resolution transmission electron microscopy (HRTEM). As depicted in Fig. 3a, it can be clearly found that a few nanoparticles with a diameter of 5–10 nm are loaded on the skeletons of 3DOM materials. And from the enlarged HRTEM image (Fig. 3a'), the lattice spacing with *d* value of 0.223 nm can be clearly observed, which is very close to the (111) plane of the standard Pt sample (JCPDS Card No. 87-0640), indicating that Pt nanoparticles are uniformly and compactly grew on the skeleton surface of 3DOM-WO₃. While the *d* value of 3DOM-WO₃ was estimated to be 0.378 nm, in good agreement with the information on the (020) plane of WO₃. However, the obvious difference can be observed when the 3DOM-WO₃/Pt was vulcanized by H₂S. In Fig. 3b', c', d', e', f', the HRTEM images show that a typical layered WS₂ with an interplanar distance of 0.616 nm are covered on the surface of 3DOM-WO₃/Pt samples, which is consistent with the *d*-spacing of the (002) planes of WS₂. Particularly, for the WOS-1 sample, only monolayer WS₂ can be clearly observed, which is tightly coated on the outer surface of 3DOM-WO₃/Pt. More importantly, with increase of the loading amount of sulfur powder, the layer numbers of WS₂ in the Z-scheme heterojunction is found to be increased gradually. It can be observed that the average numbers of WS₂ layer in WOS-2, WOS-3 and WOS-4 samples are 2–3, 4–5 and 6–7, respectively. Meanwhile, the content of S element in these Z-scheme heterojunction is also gradually increased, which can be detected by the EDX spectra in Fig. S1. Additionally, all the HRTEM images in Fig. 3 show that the Pt NPs are

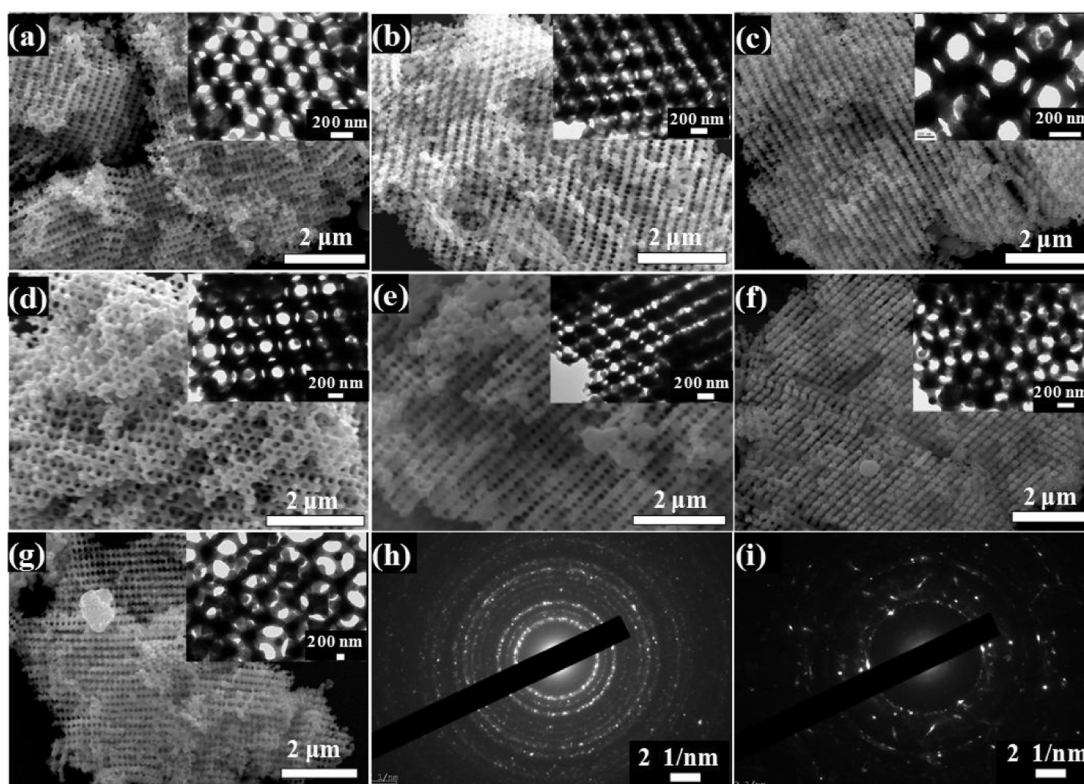


Fig. 2. SEM images of the obtained samples: (a) 3DOM-WO₃, (b) 3DOM-WO₃/Pt, (c) WOS-1, (d) WOS-2, (e) WOS-3, (f) WOS-4, (g) 3DOM-WO₃/Pt/WS₂; (Insets are TEM images of corresponding samples, respectively.) The selected area electron diffraction patterns: (h) 3DOM-WO₃ and (i) WOS-2.

grew at the interface between WS₂ and WO₃. As we all know, this spatial distribution of above composite material completely meets the description of Z-scheme heterojunction, which can vastly promote the photogenerated charges transfer and separation [41,42].

In order to better understand the relationship between photocatalytic activity and layer number of WS₂ coated on the surface of 3DOM-WO₃/Pt, the photocatalytic degradation of RhB solution was performed under Vis-NIR light irradiation. As shown in Fig. 4a, pure 3DOM-WO₃, 3DOM-WO₃/Pt and 3DOM-WO₃/Pt/WS₂ samples show poor photocatalytic activity in a short period of time. As expected, all the Z-scheme heterojunctions of 3DOM-WO₃/Pt/WS₂ exhibit wonderful photocatalytic activity. Particularly, the WOS-2 sample coated by 2–3 layers WS₂ shows the highest photocatalytic activity and excellent chemical stability (Fig. 4c), and its degradation rate of RhB can be reached to 99.2% after 30 min photoreaction, which is about 50 times and 210 times higher than that of 3DOM-WO₃/Pt and 3DOM-WO₃/Pt/WS₂, respectively. However, in comparison with the WOS-2 sample, by increasing or decreasing the layer numbers of WS₂, the photocatalytic activities of 3DOM-WO₃/Pt/WS₂ Z-scheme heterojunctions are more or less decreased. The results have also been proofed by the reaction kinetics curve (Fig. 4b), which is well followed a pseudo-first order dynamics model. According to above analysis, it is confident that the average numbers of WS₂ layer in the Z-scheme system play a key role in the enhancing photocatalytic activity. So, the phase composition, crystalline structure, porous architecture, optoelectronic property and light absorption of the obtained samples have been systematically investigated in the below sections.

As shown in Fig. 5a, the pure 3DOM-WO₃ and 3DOM-WO₃/Pt show the same routine visible light responsive ability with the absorption edge up to 491 nm and its corresponding bandgap is 2.72 eV. By contrast, the pure 3DOM-WO₃/Pt sample shows the strongest light absorption ability with a very broad and flat absorption tail that spreads across much of visible and near infrared light region down to 800 nm. Thus, it is no surprised that coating different numbers of WS₂ layers on

the skeleton of 3DOM-WO₃/Pt can significantly increase their light absorption in the visible and near infrared region. In addition, the WOS-1 and WOS-2 samples have clear absorption edge, which can be inferred by the transformed Kubelka-Munk function that their bandgap are about 2.31 eV and 1.75 eV, respectively (Fig. 5b) [43]. Moreover, although the bandgap of WOS-3, WOS-4 and 3DOM-WO₃/Pt/WS₂ are hard to calculate because the absorption edge is difficulty to be observed, the previous studies have been reported that the pure bulk WS₂ has the narrow bandgap of 1.4 eV [5]. On basis of the above analysis, it can be concluded that the bandgap of heterojunction materials monotonically increases from 1.4 eV (3DOM-WO₃/Pt/WS₂) to about 2.31 eV (WOS-1). Moreover, it should be noted that there is no absorption peak can be observed between the wavelength of 500 nm and 600 nm in Fig. 5a, indicating that the Pt NPs in the 3DOM-WO₃/Pt/WS₂ system cannot produce localized surface plasmon resonance to influence the light absorption performance [44–47].

As shown in Fig. 6a, the photocurrent density of 3DOM-WO₃, 3DOM-WO₃/Pt and 3DOM-WO₃/Pt/WS₂ show much poor photocurrent transient response due to their weak separation efficiency of the photoexcited charge carriers. When coating WS₂ on the surface of 3DOM-WO₃/Pt, the WOS-2 sample exhibits the strongest photocurrent response signals. However, under visible light irradiation, the photocurrent intensities of the resultant composites decreased with the illumination time increasing. This is due to the fact that the Nafion proton exchange membrane is unstable under visible light irradiation rather than the stability of catalyst was destroyed [48]. In the meanwhile, the diameter of the Nyquist circle of WOS-2 (Fig. 6b) is also much smaller than that of pure 3DOM-WO₃, 3DOM-WO₃/Pt and 3DOM-WO₃/Pt/WS₂, demonstrating that the 3DOM-WO₃/Pt coated by 2–3 layer WS₂ possesses ultrahigh electron conductivity and mobility, leading to more effective separation of electron-hole pairs [49,50]. In order to further evaluate the separation efficiency of electron-hole pair, the photoluminescence (PL) spectra of the synthesized samples were studied. As shown in Fig. 6c, all the samples show a broad emission peaks in

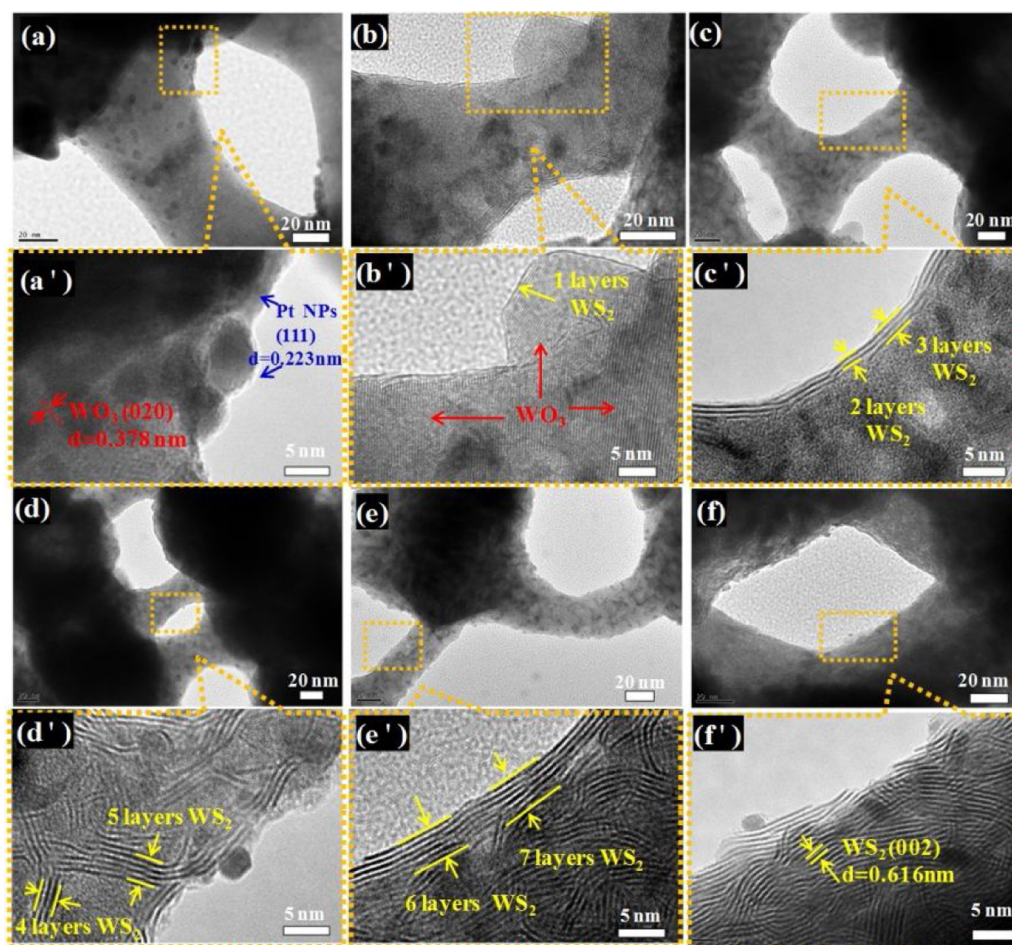


Fig. 3. High-resolution TEM (HRTEM) images of 3DOM-WO₃/Pt (a-a'), WOS-1 (b-b'), WOS-2 (c-c'), WOS-3 (d-d'), WOS-4 (e-e'), 3DOM-WS₂ (f-f').

wavelength of 473 nm when these materials were excited in wavelength of 325 nm. In the case of 3DOM-WO₃ and 3DOM-WO₃/Pt, both of them have the closed intense PL emission peak, suggesting that the high recombination ability of excited electron-hole pairs. However, when 3DOM-WO₃/Pt was coated by mono- or few-layered WS₂, the WOS-2 sample shows a significantly weak emission peak at the same position, suggesting that the separation of electron-hole pairs is significantly enhanced in the as-formed 3DOM Z-scheme heterojunction. In Fig. 6d and table S1, the time-resolved fluorescence decay spectra further illustrate the advantages of coating few-layered WS₂ on the surface of 3DOM-WO₃/Pt for the improvement of charge separation. Both the short lifetime (τ_1) and long lifetime (τ_2) for WOS-2 sample are vastly increased, indicating that 3DOM-WO₃/Pt/WS₂ possesses much longer lifetime of photogenerated charge carriers than those of 3DOM-WO₃/Pt and 3DOM-WS₂/Pt, in good accordance with the above analysis in Fig. 6a–c.

Fig. 7a shows the XRD patterns of the as-prepared samples. All the diffraction peaks presented in the XRD data can be well indexed to the crystalline phases of WO₃ (JCPDS Card No. 71-0131) and WS₂ (JCPDS Card No. 84-1398), respectively. No obvious characteristic peaks of Pt nanoparticles are observed due to its low concentration. In addition, the 3DOM-WO₃ and 3DOM-WO₃/Pt samples show intense and sharp (002) main peaks, indicative of high degree of crystallinity. With the increase of the layered WS₂ loading, the intensity of the (002) main peaks from WOS-1 to WOS-4 sample become weak gradually, suggesting that the all-solid-state Z-scheme structure is successfully constructed. Especially, no obvious diffraction peaks of WO₃ can be observed in the 3DOM-WS₂/Pt sample, which means that the 3DOM-WO₃/Pt have been completely changed into 3DOM-WS₂/Pt when the sulfur powder was

exceeded the desired amount.

The N₂ adsorption-desorption isotherms and the pore size distribution curves of the 3DOM-WO₃ and WOS-2 are shown in Fig. 7b. It can be seen that both of the samples display typical type-IV isotherms with H3 hysteresis loop in the relative pressure (p/p_0) range of 0.4–1.0, indicating that the presence of macroporous structure in these samples [51]. In addition, the two samples present similar pore size distribution curves, and the pore sizes are centered in the range of 2–12 nm, further confirming that the existence of abundant mesoporous structure in the 3DOM Z-scheme system. Table S2 summarized the texture parameters of 3DOM-WO₃ and WOS-2 sample, respectively. The WOS-2 sample shows higher BET surface area of 19.42 m²/g and lower average pore size of 8.33 nm than that of 3DOM-WO₃ (15.34 m²/g for surface area and 12.31 nm for average pore size). The BET results show that this kind of 3DOM hierarchical structure with high active surface area is favorable for the mass transfer and reactant enrichment, as result of leading to the enhancement of photocatalytic activity.

To further examine the chemical components and electronic states of elements in the 3DOM-WO₃/Pt/WS₂ all-solid-state Z-scheme heterojunction, the X-ray photoelectron spectroscopy (XPS) measurement was performed. In Fig. 8a, it is clearly found that two peaks are located at the high binding energies of 38.42 eV and 36.25 eV, it can be assigned to W 4f_{7/2} and W 4f_{5/2}, respectively, which derived from W⁶⁺ in WO₃. In the meanwhile, the fitting results show that there are another two peaks appeared at the low binding energies of 35.22 eV and 33.08 eV, which can be indexed to W 4f_{5/2} and W 4f_{7/2} from W⁴⁺ in WS₂. The results indicate that the S has partially replaced O in the surface of WO₃ to form the WS₂ in the all-solid-state Z-scheme composites. Fig. 8b shows the high-resolution S 2p XPS spectra. Two peaks of S 2p_{3/2} and S

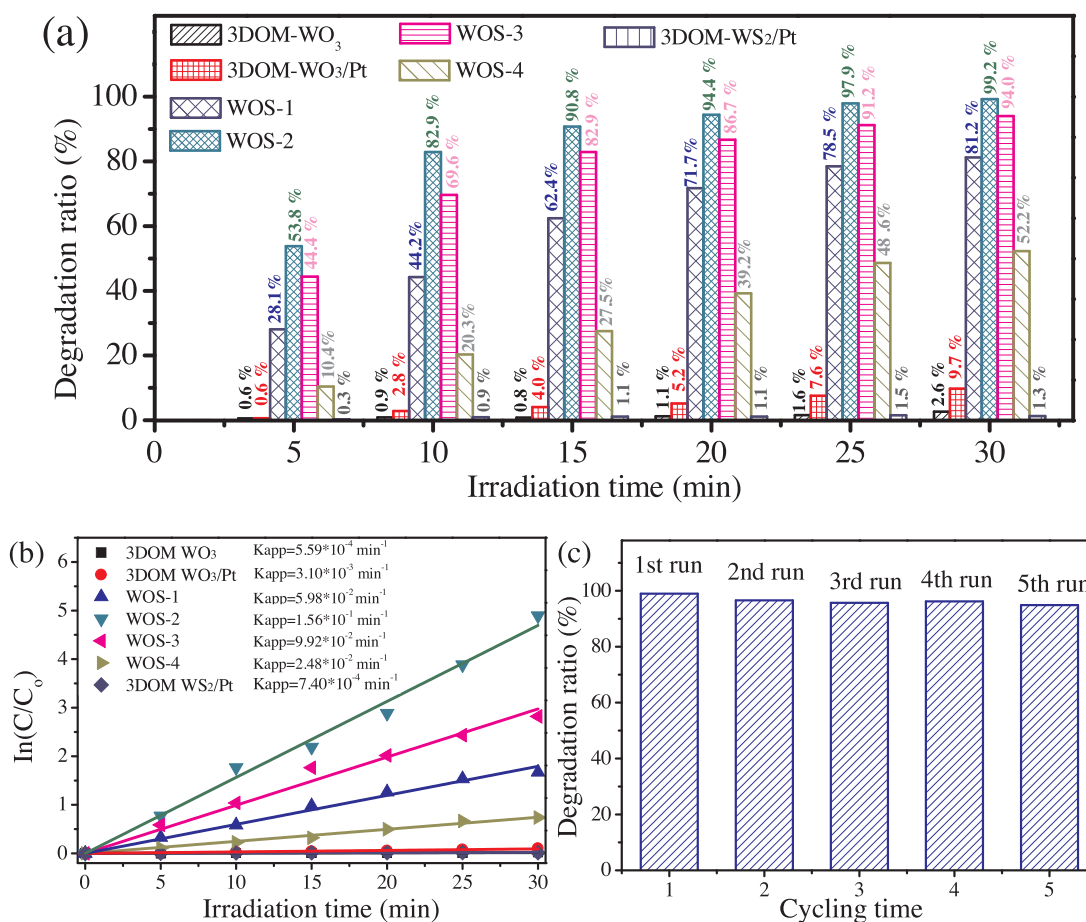


Fig. 4. (a) Plots of the decomposition of RhB solution under Vis-NIR light irradiation ($\lambda \geq 420$ nm), (b) plots of $\ln(C_0/C)$ versus irradiation time in degrading of RhB solution, (c) recycling degradation curve of WOS-2 for 5 runs. Reaction conditions: 30 mg photocatalyst, 60 mL of 30 mg/L RhB.

$2p_{1/2}$ located at the binding energy of 162.69 eV and 163.71 eV can be attributed to the presence of S^{2+} in WS_2 [52], and the peak at 169.33 eV can be assigned to S^{6+} , which is ascribed to the oxidation of divalent sulfide ions [17]. In Fig. 8c, the peak of O 1s at the binding energy of 530.52 eV was characteristic of the lattice oxygen in WO_3 . As shown in Fig. 8d, Pt 4f spectrum presents two specific peaks at 75.75 eV and 72.40 eV, which can be attributed to the Pt $4f_{5/2}$ and Pt $4f_{7/2}$, respectively. Besides, X-ray photoelectron spectroscopy (XPS) measurements are also powerful tool to further identify the contents in the sample. From the XPS survey spectra (Fig. 8), the atomic relative concentration of metallic Pt in 3DOM- WO_3 /Pt/ WS_2 Z-scheme heterojunctions (WOS-2) was calculated to be 1.0 at%.

The investigation of main reactive species involved in the

photocatalytic degradation of RhB is vital to understand the real charges participating in photo-reactive process in the 3DOM- WO_3 /Pt/ WS_2 Z-scheme system. In this work, the lactic acid, benzoquinone and isopropyl alcohol were respectively used to trapped the reactive species of the holes (h^+), superoxide radical anions ($\cdot O_2^-$) and hydroxyl radicals ($\cdot OH$). As shown in Fig. 9, the photocatalytic activity of decomposing RhB almost has no change when 3 mL isopropyl alcohol adding. On the contrary, after adding lactic acid and benzoquinone in the photoreaction system, the activity over WOS-2 sample was declined clearly. These experimental results suggest that the formed $\cdot O_2^-$ and photogenerated h^+ are the main reactive species for RhB removal over WOS-2 sample.

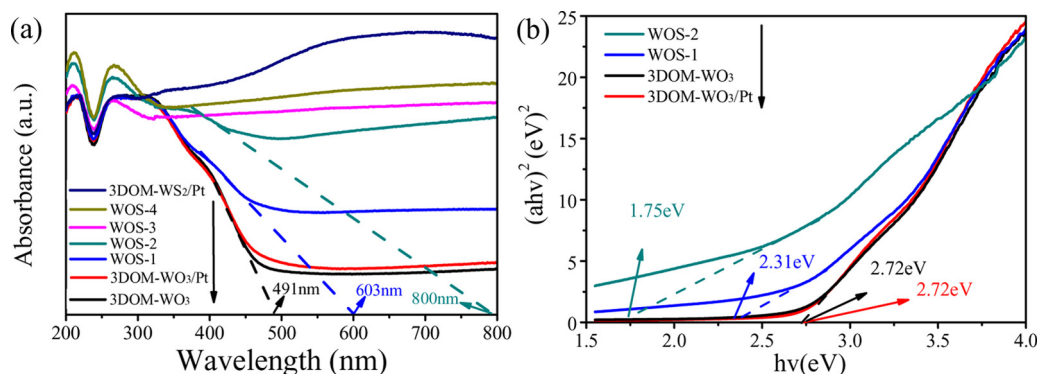


Fig. 5. (a) UV-vis diffuse reflectance spectra (DRS) and (b) plots of $(ah\nu)^{1/2}$ versus energy ($h\nu$) for 3DOM- WO_3 , 3DOM- WO_3 /Pt, WOS-1 and WOS-2.

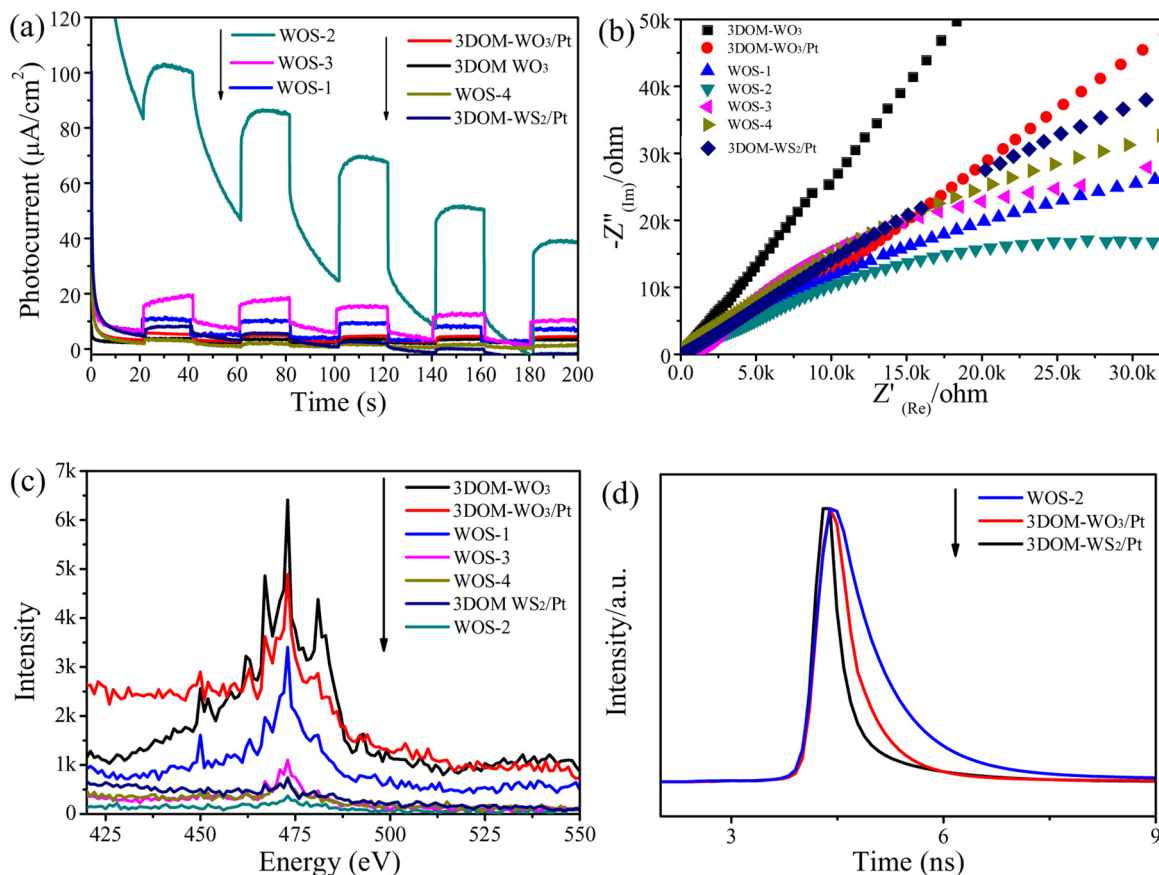


Fig. 6. (a) Transient photocurrent density, (b) electrochemical impedance spectroscopy (EIS) Nyquist plots and (c) PL spectra of the sample of 3DOM-WO₃, 3DOM-WO₃/Pt and 3DOM-WO₃/Pt/WS₂ composites with different WS₂ layers, (d) Time-resolved fluorescence decay spectra of 3DOM-WO₃/Pt, 3DOM-WS₂/Pt and WOS-2.

4. Discussion

From the aforementioned analysis, it can be deduced that the main reactive species of $\cdot\text{O}_2^-$ and h^+ triggered the photoreaction over the as-prepared 3DOM-WO₃/Pt/WS₂ sample. Hence, identification of actual photogenerated charges transfer routes at interface between WO₃ and WS₂ via Pt NPs “bridge” is necessary and beneficial for further understanding the tentative mechanism for the photodegradation activity of RhB in the 3DOM Z-scheme heterojunction. Recently, the selective photo-deposited noble metal Au nanoparticles on the as-obtained 3DOM-WO₃/Pt/WS₂ catalysts is considered to be one of effective ways to testify the path of electrons transfer between WS₂ and WO₃ [53,54]. In this work, 3 wt% $\text{AuCl}_3\cdot\text{HCl}\cdot 4\text{H}_2\text{O}$, as the electron acceptor, was added into the system during the photoreaction performing, and

the Au^{3+} can be quickly reduced into Au nanoparticles under visible light irradiation and finally loaded on the surface of the as-formed Z-scheme samples. Fig. 10 shows the TEM and HRTEM images for the series of 3DOM-WO₃/Pt/WS₂ samples with photo-deposited Au nanoparticles. It can be seen from Fig. 10 a, d, g, j that lots of metal nanoparticles were randomly distributed on the surfaces of 3DOM catalysts. Further observation of the HRTEM images for the 3DOM-WO₃/Pt/WS₂ samples (Fig. 10 b, e, h, c, f, i), it is obvious that most of Au nanoparticles with size of 2–3 nm were photo-reduced by visible light and contacted tightly around the Pt nanoparticles, and the similar results can further be proved by the EDX elemental mapping spectroscopy of WOS-2 sample (Fig. S2). And these abovementioned results can be intuitively proved that the photogenerated charges in the as-prepared 3DOM heterojunction are transferred according to the Z-scheme

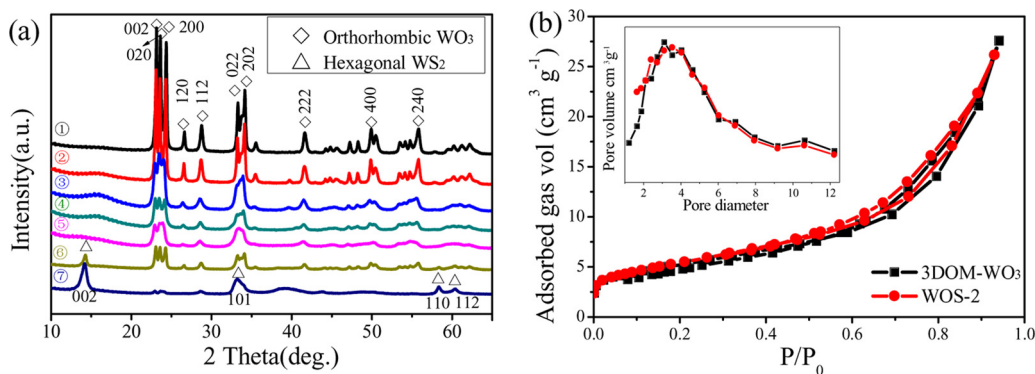


Fig. 7. (a) XRD patterns of ① 3DOM-WO₃, ② 3DOM-WO₃/Pt, ③ WOS-1, ④ WOS-2, ⑤ WOS-3, ⑥ WOS-4, ⑦ 3DOM-WS₂/Pt samples. (b) N₂ adsorption-desorption isotherms and the corresponding pore size distributions curve (the inset of b) of 3DOM-WO₃ and WOS-2 sample.

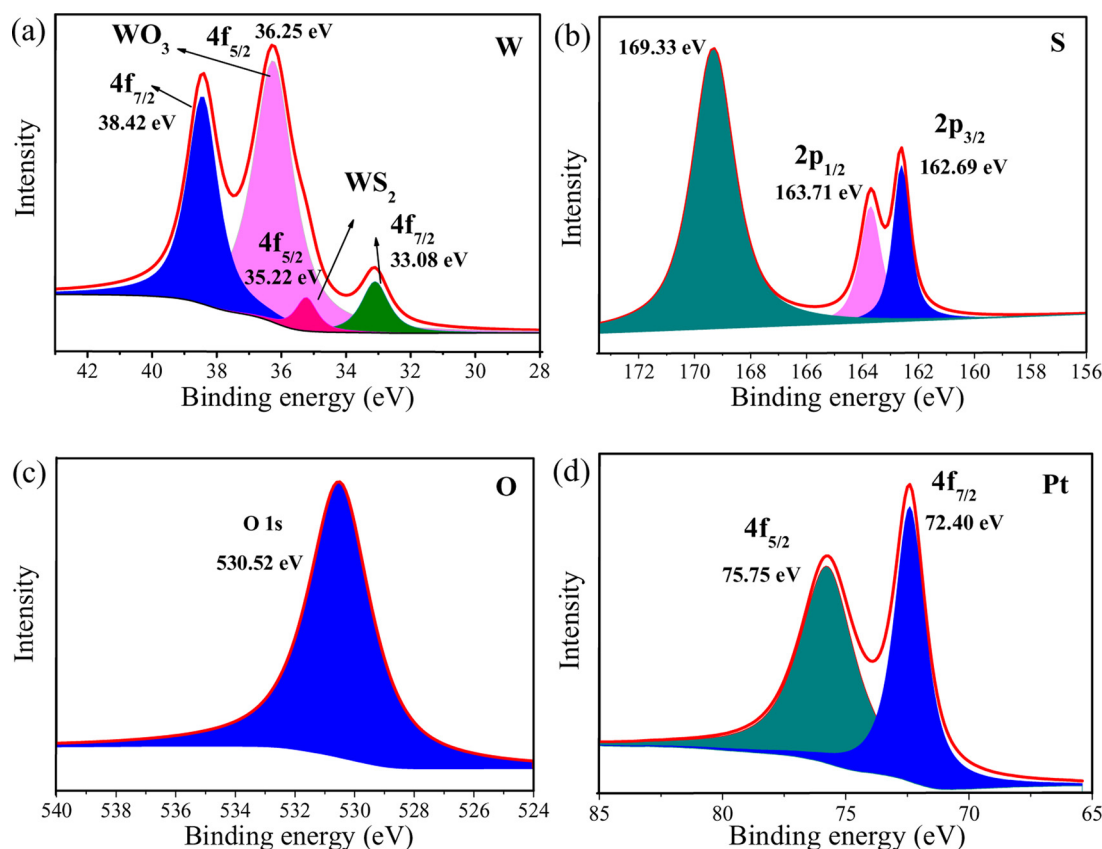


Fig. 8. XPS spectra of WOS-2 sample, W 4f (a), S 2p (b), O 1s (c) and Pt 4f (d).

mechanism, which will be discussed later. Furthermore, when the layered number of WS_2 coated on the skeletons of $3\text{DOM-}\text{WO}_3/\text{Pt}/\text{WS}_2$ sample were increased, some interesting situation can be found: the amount of Au nanoparticles photo-deposited around Pt surface were firstly increased to the maximum value from WOS-1 sample to WOS-2 sample, and then gradually decreased, especially for WOS-4 sample, it is hard to observe the photo-deposited Au nanoparticles (Fig. 10k and l). The results of selective photo-deposition of noble metal Au directly confirm that the layer numbers of WS_2 deliver the different charge separation efficiency, and thus it can be concluded that the WOS-2 sample possesses high charge separation ability, leading to the highest photocatalytic activity of RhB decomposition. While the WOS-4 sample with rapid interfacial charge recombination rate restricts the enhancement of its catalytic activity.

Previous studies have shown that the WS_2 with different layer numbers could produce different electronic bandgap. As illustrated in

Fig. 11a, the bulk WS_2 , as an indirect semiconductor, has the narrowest bandgap of 1.4 eV [5], but this kind of bulk WS_2 exhibits extremely low charge mobility because most of them are rapid recombination to form thermal energy during the photocatalysis process (Fig. 6). Nevertheless, with the gradual decrease of WS_2 layers numbers, the bandgap of WS_2 was gradually increased. When mono- or few-layered sample was obtained, the WS_2 will become a direct semiconductor with the widest bandgap of about 2.31 eV. It has been reported that the mono- or few-layered WS_2 exhibits higher charge mobility than that of bulk WS_2 . According to the aforementioned structure feature, in this work, we have obtained series of all-solid-state Z-scheme heterojunction through coating layered WS_2 on the skeleton of $3\text{DOM-}\text{WO}_3/\text{Pt}$ sample. Fig. 11b shows the tentative mechanism proposed for the charge transfer and separation of the $3\text{DOM-}\text{WO}_3/\text{Pt}/\text{WS}_2$ Z-scheme heterojunction. Under Vis-NIR light irradiation, both $3\text{DOM-}\text{WO}_3$ and mono or few-layered WS_2 can be excited to produce electron and hole pairs in the valence

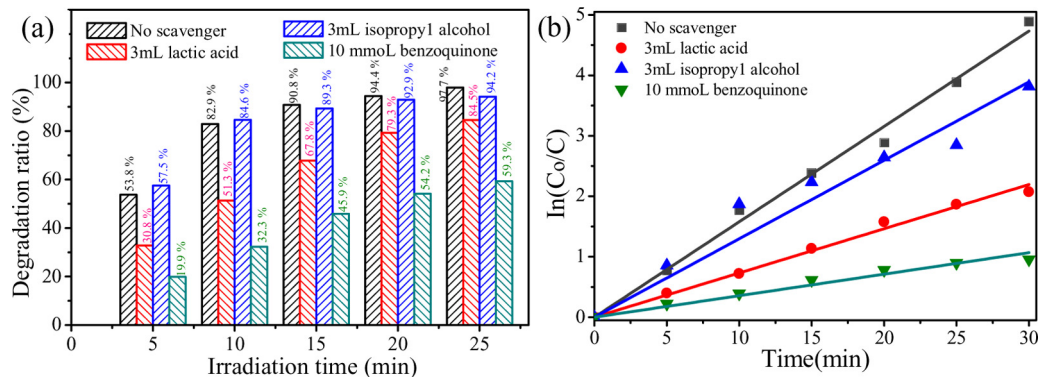


Fig. 9. (a) Plots of the decomposition of RhB solution (30 mg/mL) over WOS-2 photocatalyst with different scavengers under Vis-NIR light irradiation ($\lambda \geq 420$ nm). (b) Plots of $\ln(C_0/C)$ versus irradiation time in degrading of RhB solution. Reaction conditions: 30 mg photocatalyst, 60 mL of 30 mg/L RhB.

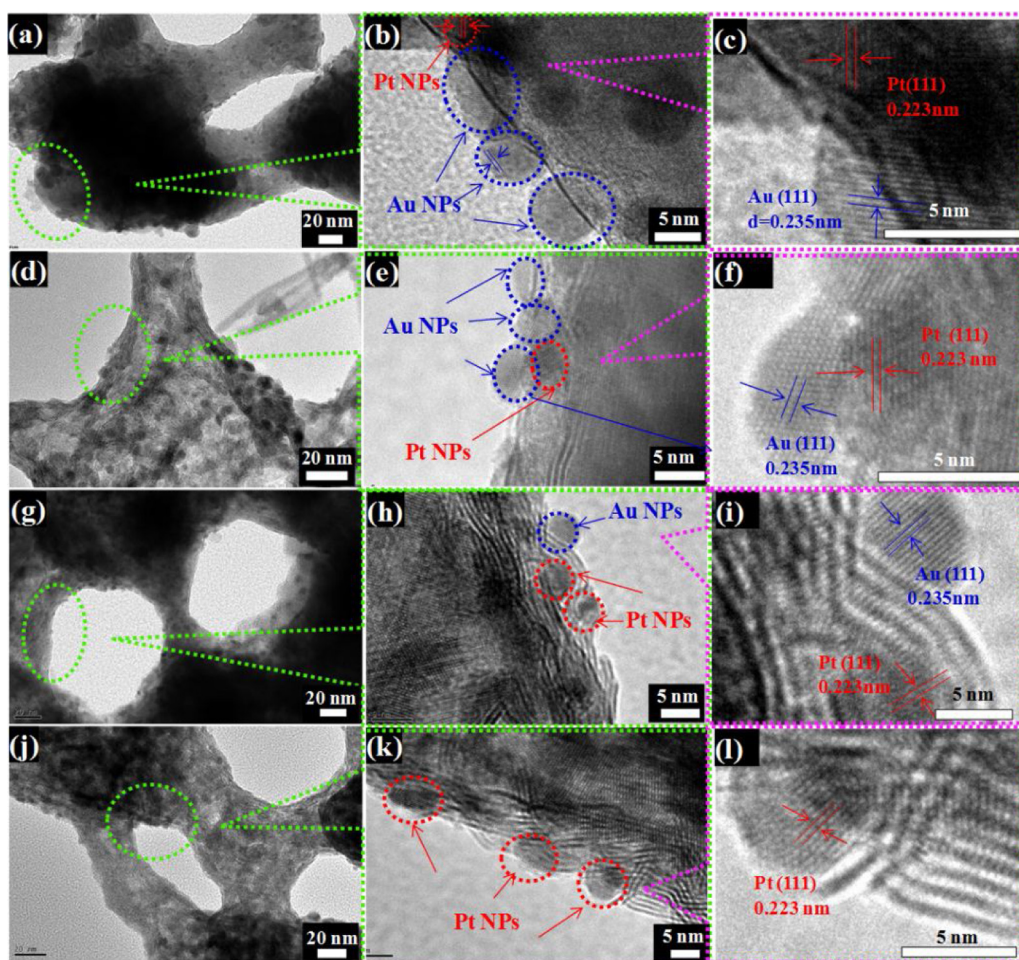


Fig. 10. TEM and HRTEM images of Photo-deposition of Au on the as-prepared samples: (a–c) WOS-1, (d–f) WOS-2, (g–i) WOS-3, (j–l) WOS-4.

band (VB) of WS_2 and WO_3 , respectively. And then the photogenerated electrons directly transfer to their conduction band (CB), respectively. Owing to the presence of numerous Pt NPs at interface between WS_2 and WO_3 , they would act as a cross-linking bridge to induce the charge separation via the Z-scheme transfer mechanism. In brief, the photo-generated electrons on the CB of WO_3 are easily transferred into metal Pt through the schottky barrier. Meanwhile, the holes on the VB of WS_2 are transferred to metal Pt, and then the recombination with electrons on the Pt surface may strongly prolong the lifetime of electron-hole in each semiconductor. After that, the photogenerated electrons on the CB of WS_2 can fastly react with oxygen to produce superoxide radical anions ($\cdot\text{O}_2^-$). Next, both the formed $\cdot\text{O}_2^-$ and the holes remain in the VB of WO_3 with strong oxidation ability as the main reactive species can effectively oxidize wastewater into CO_2 and H_2O [55–57].

In addition, a few studies have also reported that when the layer number of WS_2 is below of 4 or 5 layers, its valence band (VB) edge potentials would be more than 0.0 eV, which might lead to the H_2 evolution performance from water splitting. Therefore, the proposed Z-scheme mechanism of charge transfer in the 3DOM- $\text{WO}_3/\text{Pt}/\text{WS}_2$ sample can be further confirmed by the photocatalytic H_2 evolution experiments. It is well known that the pure WO_3 and bulk WS_2 have no the ability of producing H_2 , because the conduction band potential of WO_3 and bulk WS_2 are about 0.74 eV and 0.3 eV, respectively, which is more positive than that of water reduction potential (0.0 eV vs NHE), and thus the photogenerated electrons in conduction band of WO_3 or bulk WS_2 cannot reduce the water molecular to produce hydrogen. Hence, it is not surprise that the samples of 3DOM- WO_3/Pt and 3DOM- WS_2/Pt have no H_2 evolution activity under visible light irradiation.

However, as show in Fig. 11c, great changes are taken place when the bulk WS_2 was reduced to mono- or few-layered WS_2 . And all of the 3DOM- $\text{WO}_3/\text{Pt}/\text{WS}_2$ samples show excellent photoactivity of H_2 production, especially for the sample of WOS-2, the amount of H_2 is reached to $606 \mu\text{mol g}^{-1}$ after 5 h Vis-NIR light irradiation. This result is in good accordance with the analysis of energy band gap structure for WS_2 with different layer numbers, and also provides a strong evidence to illustrate that the Z-scheme charge transfer mechanism was occurred in the 3DOM- $\text{WO}_3/\text{Pt}/\text{WS}_2$ system. Because if the photogenerated electrons in CB of mono- or few-layered WS_2 transfer into the CB of WO_3 according to the traditional migration route of heterojunction, the WOS-2 sample would not produce the visible-light-driven H_2 generation activity at all.

Apart from the contribution of highly-efficient charge separation, the three dimensional ordered macroporous structure of the obtained novel all-solid-state Z-scheme heterojunction also plays a vital role in the enhancement of photocatalytic activity, because which not only enhances the visible light absorption based on the multi-scattering effect as well as slow photo effect but also supplies more active surface area to facilitate the mass transfer during the photocatalytic process. It is believed that all of the abovementioned factors are cooperated to endow the 3DOM- $\text{WO}_3/\text{Pt}/\text{WS}_2$ Z-scheme system highly photocatalytic performance and much better photo-stability for wastewater treatment.

5. Conclusion

In summary, the all-solid-state Z-scheme heterojunction of 3DOM- $\text{WO}_3/\text{Pt}/\text{WS}_2$ have been designed and synthesized by simple colloidal

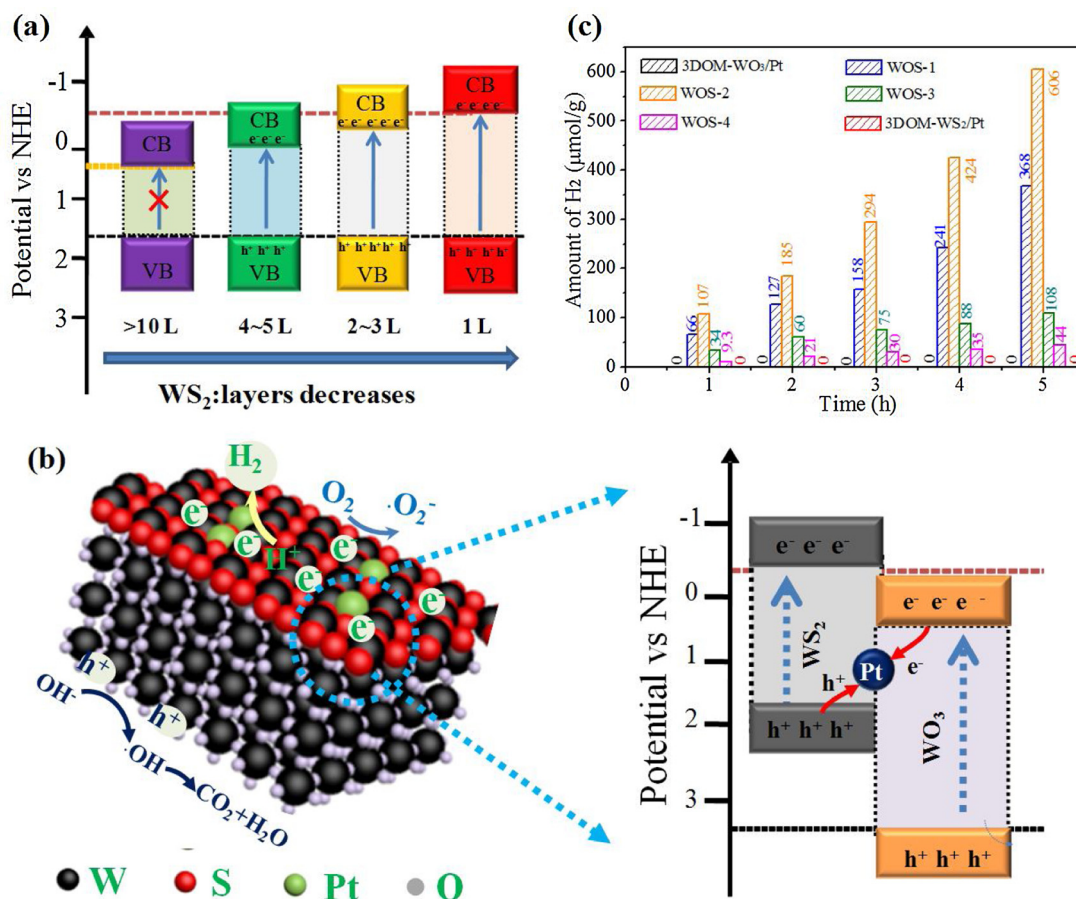


Fig. 11. (a) Energy-level diagram of WS₂ with different layers, (b) Scheme illustrating the principle of charges transfer at the interface of 3DOM-WO₃/Pt/WS₂ heterojunction. (c) Plots of photocatalytic H₂ evolution amount vs. irradiation time.

crystal-templating method assisted gas phase chemical reduction process. The bandgap of the obtained 3DOM-WO₃/Pt/WS₂ can be artificial tuned, which is ascribed to the fact that WS₂ becomes a direct semiconductor when its layer was reduced to mono-or few-layered. The systematically characterized results show that the 3DOM-WO₃/Pt/WS₂ Z-scheme heterojunctions have much higher charges separation efficiency, and thus leading to the Z-scheme heterojunction of 3DOM-WO₃/Pt coated by 2–3 layered WS₂ achieved unexpectedly photocatalytic activities and stability. In addition, the formed three-dimensionally ordered macroporous structure in the WO₃/Pt/WS₂ Z-scheme system provides a large number of interfacial reaction active sites to promote the mass transfer for photoreaction under Vis-NIR light irradiation.

Acknowledgements

This work was financially supported by the Natural Science Basic Research Plan in Shaanxi Province of China (Grant No. 2017JZ001), the National Natural Science Foundation of China (Grant No. 21303130), the Fundamental Research Funds for the Central Universities (Grant No. cxt2017004) and K. C. Wong Education Foundation, Hong Kong, China. Thanks for the technical support from International Center for Dielectric Research (ICDR), Xi'an Jiaotong University, Xi'an, China; the authors also appreciate Ms. Dai and Mr. Ma for their help in using SEM, EDX and TEM, respectively.

Appendix A. Supplementary data

Supplementary material related to this article can be found, in the online version, at doi:<https://doi.org/10.1016/j.apcatb.2018.03.068>.

References

- [1] Q.H. Wang, K. Kalantar-Zadeh, A. Kis, J.N. Coleman, M.S. Strano, *Nat. Nanotechnol.* 7 (2012) 699–712.
- [2] Y.J. Zhang, T. Oka, R. Suzuki, J.T. Ye, Y. Iwasa, *Science* 344 (2014) 725–728.
- [3] K.F. Mak, K.L. McGill, J. Park, P.L. McEuen, *Science* 344 (2014) 1489–1492.
- [4] K.F. Mak, C. Lee, J. Hone, J. Shan, T.F. Heinz, *Phys. Rev. Lett.* 105 (2010) 136805–136808.
- [5] H.S.S. Ramakrishna Matte, A. Gomathi, A.K. Manna, D.J. Late, R. Datta, S.K. Pati, C.N.R. Rao, *Angew. Chem. Int. Ed.* 49 (2010) 4059–4062.
- [6] Y.H. Sang, Z.H. Zhao, M.W. Zhao, P. Hao, Y.H. Leng, H. Liu, *Adv. Mater.* 27 (2015) 363–369.
- [7] M. Bernardi, M. Palumbo, J.C. Grossman, *Nano Lett.* 13 (2013) 3664–3670.
- [8] S. Jo, N. Ubrig, H. Berger, A.B. Kuzmenko, A.F. Morpurgo, *Nano Lett.* 14 (2014) 2019–2025.
- [9] M. Chhowalla, H.S. Shin, G. Eda, L.J. Li, K.P. Loh, H. Zhang, *Nat. Chem.* 5 (2013) 263–275.
- [10] V. Nicolosi, M. Chhowalla, M.G. Kanatzidis, M.S. Strano, J.N. Coleman, *Science* 340 (2013) 1226419.
- [11] X. Zhang, X.F. Qiao, W. Shi, J.B. Wu, D.S. Jiang, P.H. Tan, *Chem. Soc. Rev.* 44 (2015) 2757–2785.
- [12] Y. Zhong, G. Zhao, F. Ma, Y. Wu, X. Hao, *Appl. Catal. B: Environ.* 199 (2016) 466–472.
- [13] D. Voiry, H. Yamaguchi, J. Li, R. Silva, D.C.B. Alves, T. Fujita, M. Chen, T. Asefa, V.B. Shenoy, G. Eda, M. Chhowalla, *Nat. Mater.* 12 (2013) 850–855.
- [14] F.N. Xia, H. Wang, D. Xiao, M. Dubey, A. Ramasubramanian, *Nat. Photon.* 8 (2014) 899–907.
- [15] Y.C. Liu, Y.P. Zhao, L.F. Jiao, J. Chen, *J. Mater. Chem. A* 2 (2014) 13109–13115.
- [16] E. Yang, H. Ji, Y.S. Jung, *J. Phys. Chem. C* 119 (2015) 26374–26380.
- [17] P. Zhou, Q. Xu, H. Li, Y. Wang, B. Yan, Y. Zhou, J. Chen, J. Zhang, K. Wang, *Angew. Chem. Int. Ed.* 54 (2015) 15226–15230.
- [18] S.Z. Butler, S.M. Hollen, L. Cao, Y. Cui, J.A. Gupta, H.R. Gutierrez, T.F. Heinz, S.S. Hong, J. Huang, A.F. Ismach, J.H. Ezekiel, M. Kuno, V.V. Plashnitsa, R.D. Robinson, R.S. Ruoff, S. Salauddin, J. Shan, L. Shi, M.G. Spencer, M. Terrones, W. Windl, J.E. Goldberger, *ACS Nano* 7 (2013) 2898–2926.
- [19] W.J. Zhao, Z. Ghorannevis, L.Q. Chu, M. Toh, C. Kloc, P.H. Tan, G. Eda, *ACS Nano* 7 (2012) 791–797.
- [20] X.F. Qiao, X.L. Li, X. Zhang, W.J. Shi, B. Wu, T. Chen, P.H. Tan, *Appl. Phys. Lett.*

- 106 (2015) 223102–223106.
- [21] X.L. Li, W.P. Han, J.B. Wu, X.F. Qiao, J. Zhang, P.H. Tan, *Adv. Funct. Mater.* 27 (2017) 1604468–1604491.
- [22] L. Liu, S.B. Kumar, Y. Ouyang, J. Guo, *IEEE Trans. Electron Devices* 58 (2011) 3042–3047.
- [23] R. Morrish, T. Haak, C.A. Wolden, *Chem. Mater.* 26 (2014) 3986–3992.
- [24] L.J. Zhang, S. Li, B.K. Liu, D.J. Wang, T.F. Xie, *ACS Catal.* 4 (2014) 3724–3729.
- [25] H. Tada, T. Mitsui, T. Kiyonaga, T. Akita, K. Tanaka, *Nat. Mater.* 5 (2006) 782–786.
- [26] L. Yang, X.B. Zhu, S.J. Xiong, X.L. Wu, Y. Shan, P.K. Chu, *ACS Appl. Mater. Interfaces* 8 (2016) 13966–13972.
- [27] Z.G. Zhao, M. Miyauchi, *Angew. Chem. Int. Ed.* 120 (2008) 7159–7163.
- [28] X.Q. Yan, K. Ye, T.X. Zhang, C. Xue, D. Zhang, C.S. Ma, J.J. Wei, G.D. Yang, *New J. Chem.* 41 (2017) 8482–8489.
- [29] T. Wang, X.Q. Yan, S.S. Zhao, B. Lin, C. Xue, G.D. Yang, S.J. Ding, B.L. Yang, C.S. Ma, G. Yang, G.R. Yang, *J. Mater. Chem. A* 2 (2014) 15611–15619.
- [30] C. Xue, T. Wang, G. Yang, B.L. Yang, S.J. Ding, *J. Mater. Chem. A* 2 (2014) 7674–7679.
- [31] M. Sadakane, K. Sasaki, H. Kunioku, B. Ohtani, W. Ueda, R. Abe, *Chem. Commun.* (2008) 6552–6554.
- [32] K. Ji, H. Arandiyan, P. Liu, L. Zhang, J.H. Han, Y.C. Xue, J.G. Hou, H.X. Dai, *Nano Energy* 27 (2016) 515–525.
- [33] Y. Chang, K. Yu, C.X. Zhang, R. Li, P.Y. Zhao, L.L. Lou, S.X. Liu, *Appl. Catal. B: Environ.* 176 (2015) 363–373.
- [34] C. Xue, H. An, X.Q. Yan, J.L. Li, B.L. Yang, J.J. Wei, G.D. Yang, *Nano Energy* 39 (2017) 513–523.
- [35] B. Lin, C. Xue, X.Q. Yan, G.D. Yang, G. Yang, B.L. Yang, *Appl. Surf. Sci.* 357 (2015) 346–355.
- [36] C. Xue, X. Xu, G.D. Yang, S.J. Ding, *RSC Adv.* 5 (2015) 102228–102237.
- [37] Y. Huang, Y.L. Liang, Y.F. Rao, D.D. Zhu, J.J. Cao, Z.X. Shen, W.K. Ho, S.C. Lee, *Environ. Sci. Technol.* 51 (2017) 2924–2933.
- [38] M. Sadakane, C. Takahashi, N. Kato, H. Ogihara, Y. Nodasaka, Y. Doi, Y. Hinatsu, W. Ueda, *Bull. Chem. Soc. Jpn.* 80 (2007) 677–685.
- [39] X.Q. Yan, C. Xue, B.L. Yang, G.D. Yang, *Appl. Surf. Sci.* 394 (2017) 248–257.
- [40] J.C. Lytle, N.R. Denny, R.T. Turgeon, A. Stein, *Adv. Mater.* 19 (2007) 3682–3686.
- [41] Z.H. Wang, X.X. Fan, D.M. Han, F.B. Gu, *Nanoscale* 8 (2016) 10622–10631.
- [42] Y. Sang, Z. Zhao, M. Zhao, P. Hao, Y. Leng, H. Liu, *Adv. Mater.* 27 (2015) 363–369.
- [43] W. Gao, M. Wang, C. Ran, X. Yao, H. Yang, J. Liu, D. He, J. Bai, *Nanoscale* 6 (2014) 5498–5508.
- [44] T.X. Lu, B.X. Li, Y.G. Hao, F. Han, L.L. Zhang, L.Y. Hu, *Appl. Catal. B: Environ.* 165 (2015) 378–388.
- [45] B.X. Li, T. Gu, T. Ming, J.X. Wang, P. Wang, J.F. Wang, J.C. Yu, *ACS Nano* 8 (2014) 8152–8162.
- [46] B.X. Li, Y.G. Hao, X.K. Shao, H.D. Tang, T. Wang, J.B. Zhu, S.L. Yan, *J. Catal.* 329 (2015) 368–378.
- [47] B.X. Li, X.K. Shao, T.X. Lu, L.Z. Shao, B.S. Zhang, *Appl. Catal. B: Environ.* 198 (2016) 325–333.
- [48] C. Xue, T.X. Zhang, S.J. Ding, J.J. Wei, G.D. Yang, *ACS Appl. Mater. Interfaces* 9 (2017) 16091–16102.
- [49] Y. Feldman, E. Wasserman, D.J. Srolovitz, R. Tenne, *Science* 267 (1995) 222.
- [50] N. Li, L. Feng, D. Li, J. Su, Z. Liu, *Mater. Des.* 92 (2016) 129–134.
- [51] L.Q. Ye, J.Y. Liu, C.Q. Gong, L.H. Tian, T.Y. Peng, L. Zan, *ACS Catal.* 2 (2012) 1677–1683.
- [52] P. Zhou, J. Yu, M. Jaroniec, *Adv. Mater.* 26 (2014) 4920–4935.
- [53] C. Han, Z. Chen, N. Zhang, J.C. Colmenares, Y.J. Xu, *Adv. Funct. Mater.* 25 (2015) 221–229.
- [54] B. Lin, G.D. Yang, B.L. Yang, Y.X. Zhao, *Appl. Catal. B: Environ.* 198 (2016) 276–285.
- [55] Y. Huang, W.K. Ho, S.C. Lee, L.Z. Zhang, G.S. Li, J.C. Yu, *Langmuir* 24 (2008) 3510–3516.
- [56] D. Voiry, H. Yamaguchi, J.W. Li, R. Silva, D.C.B. Alves, T. Fujita, M.W. Chen, T. Asefa, V.B. Shenoy, G. Eda, M. Chhowalla, *Nat. Mater.* 12 (2013) 850–855.
- [57] R. Li, F. Zhang, D. Wang, J. Yang, M. Li, J. Zhu, X. Zhou, H. Han, C. Li, *Nat. Commun.* 4 (2013) 1432–1438.